A benchmark study for the crown-type splashing dynamics of two-component droplet-wall film interactions

A. Geppert[a,*], A. Terzis[a], G. Lamanna[a,*], M. Marengo[b], B. Weigand[a]

[a] *Institute of Aerospace Thermodynamics, Universität Stuttgart, Pfaffenwaldring 31, D-70569 Stuttgart, Germany*
[b] *School of Computing, Engineering and Mathematics, University of Brighton, Cockcroft Building, Lewes Road, Brighton BN2 4GJ, UK*

Abstract

The present paper investigates experimentally the splashing dynamics of two-component droplet wall film interactions. Over a wide range of Weber numbers and dimensionless film thickness, the different combinations of two low surface tension fluids, e.g. hexadecane and hyspin, including their corresponding one-component interactions, have been considered. As a first step, the splashing morphology is examined and the respective similarities with open literature data are reported. In addition, the splashing dynamics is investigated evaluating quantitatively the time evolution of crown height and diameter, the total number of liquid jets (fingers) generated at the upper crown rim as well as the total number of ejected secondary droplets including their corresponding diameter, cumulative volume and velocity magnitude. The results are analysed by various post-processing procedures aiming to provide a large dataset, which can be efficiently used for the validation of numerical models. Furthermore, the importance of the impact morphology for understanding the impact dynamics is pointed out.

Keywords: droplet dynamics, drop film interaction, secondary droplets, crown-type splashing

1. Introduction

The impact of droplets onto thin liquid films finds great applicability in a variety of natural and industrial processes such as rain erosion, extinguishing film fuelled fires, spray cooling, fuel injection in engines or spray freeze drying. A considerable amount of research has been therefore focused on the impact morphology of droplet wall-film interactions, e.g. reviews can be found in Liang and Mudawar [18], Moreira et al. [19] or Yarin [32]. Among different impact morphologies [25, 26], *splashing* has drawn great scientific interest due to its relatively complex and fascinating features such as jets (liquid fingers) originating from the upper crown rim, secondary droplet ejection or (partial) dewetting of the surface. The splashing morphology can

*corresponding author. Tel.: +49 (0) 711 685-62173
Email addresses: anne.geppert@itlr.uni-stuttgart.de (A. Geppert), grazia.lamanna@itlr.uni-stuttgart.de (G. Lamanna)

be characterized by the dynamics of the impacting drop (D diameter, U impact velocity), by the liquid properties (viscosity μ, density ρ, surface tension σ) and by the film thickness h. Thereof, three dimensionless numbers are defined: the Weber number $We = (\rho U^2 D)/(\sigma)$, the Ohnesorge number $Oh = \mu/(\sqrt{D\rho\sigma})$ and the dimensionless film thickness $\delta = h/D$. The evolution in time can be defined by the non-dimensional time $\tau = (Ut)/D$. According to Cossali et al. [4] two kinds of splashing need to be considered: the *prompt splash*, which is related to an early ejection of secondary droplets during the ascending phase of the crown. The late splash, also called corona splash or *crown-type splash*, is characterised by the formation of liquid fingers along the upper crown rim and their subsequent disintegration into secondary droplets. This secondary atomisation takes place when the crown is fully developed. Note that both kinds of splashing can occur during one impact event [29], however viscosity and surface tension influence which splashing type is predominant. For low and high Ohnesorge numbers prompt and crown-type splash take place, respectively [20, 4]. Regarding the influence of liquid properties on splashing, Vander Wal et al. [29] carried out an extensive experimental study, reporting that high surface tension and viscosity hinder splashing for droplet impact on thin films. This is in agreement with Cossali et al. [4], who found that higher surface tension and viscosity require more impact energy for splashing. They also deduced a correlation for the onset of splashing from their experimental study. Such formulations, describing the threshold for the onset of splashing, and hence secondary droplet formation, are essential for investigating splashing mechanisms. A common choice is the non-dimensional group $K = We^x Oh^y$, also referred to as *impact factor*, which takes into account the effects of impacting kinetic energy, surface tension and viscous forces. In literature two types of correlations are available: The first type solely depends on We and Oh ([30, 23, 24, 33, 31]), while the second one takes into account the film thickness, [8, 7, 20, 14, 28, 4].

Geppert et al. [8] recently published a splashing correlation for hexadecane one-component interactions ($We^{5/8}\ Oh^{-1/4} = 114 + 165\ \delta^{6/5}$) and mapped the observed impact morphology. The obtained morphology mapping is revived here, because the observed phenomenon of bubble formation in the splashing regime strongly influences the results presented later on. According to [8], it occurs when the respective thresholds for the Weber number (i.e., $We > 1100$) and the dimensionless film thickness (i.e., $\delta \geq 0.2$) are exceeded. The formation process itself starts during the receding phase of the crown, when the crown rim grows thicker and begins to contract until a temporarily stable bubble is formed. During the contraction of the rim the liquid fingers merge, reducing the number of ejected secondary droplets and increasing their size.

[Figure 1 about here.]

In the splashing regime, Deegan et al. [6] identified three sources for secondary droplet formation: (i) prompt instability of the ejecta sheet, (ii) rim instability of the ejecta sheet and (iii) rim instability of the crown sheet, which results in jets followed by secondary droplets. The number of jets along the crown rim in the

splashing/deposition area is independent of We, δ and liquid properties (Oh), whereas inside the splashing region for thin films the number of jets increases with We [4]. Krechetnikov and Homsy [16] studied the fundamental instability behind crown formation during splash on pre-existing films. They classified three types of crowns (axisymmetric, regular and irregular) and found that the number of crown spikes (fingers) decreases with increasing film thickness. The most complete investigation of crown parameters, number of jets and secondary droplet properties with regard to their temporal evolution is presented by Cossali et al. [5]. They report that the mean size of secondary droplets increases with time for high impact velocities, while it is almost independent for low velocities. Furthermore, film thickness has a negligible influence on the secondary droplet size. Okawa et al. [23] investigated the production of secondary droplets during normal water drop impact on plane water surfaces. They chose the K-factor as appropriate scaling parameter and provided correlations for the total number of secondary droplets as well as for the ejected mass. They showed that the ejected mass increases with K, which is attributed to an increase in droplet number and droplet size. The airborne particle release due to dripping was investigated by Motzkus et al. [21, 20] employing an aerodynamic particle sizer. The authors found that inertial forces promote the emission of secondary droplets, while viscous and surface tension force hinder it, which is consistent with the effect of these forces on splashing. Additionally, they obtained the highest airborne particle mass for the lowest δ at constant We and Oh. Recently, Guildenbrecher et al. [13] introduced digital in-line holography for the determination of secondary droplet number, size, position and velocity.

Contrary to one-component droplet wall-film interactions (drop and film consist of same liquid), and despite the significant industrial interest and applicability, the amount of investigations focused on two-component impact dynamics (drop and film liquid vary) is very limited in the literature. For example, impacting fuel droplets on the cylinder surface of Diesel engines may dilute the oil lubrication performance. In addition, if the impact energy is sufficient to generate splashing, secondary droplets that consists of a combination of fuel and lubrication oil may be ejected in the combustion chamber, thus increasing dramatically the emissions of the engine. Thoroddsen et al. [27] investigated the impact of water/glycerine droplets on thin ethanol films. The authors observed thousands of small holes in the crown as a direct consequence of the surface tension difference between the drop and the film liquids that presumably result from Marangoni-driven flows and instabilities. Banks et al. [2] used water and several aqueous solutions in order to investigate the effect of droplet and wall-film viscosities on two-component droplet wall-film interactions. They found that the mechanism of crown formation strongly depends on the wall-film properties, while a small dependence of splashing on the droplet properties was also observed. In the studies of Geppert et al. [10, 9, 11, 12], various combinations between hyspin and hexadecane were investigated. The authors reported similarities about the impact outcome of one and two-component droplet wall-film interactions and a number of holes in the crown was observed for the latter case similar to Thoroddsen et al. [27]. A first correlation for the onset of splashing for two-component droplet wall-film interactions considering the Weber number of the

droplet ($We_D = \rho_D\ U^2 D/\sigma_D$), the average Ohnesorge number ($Oh_{ave} = (0.5(\mu_D + \mu_F)/\sqrt{D\rho_D\sigma_D}$) and the normalised wall-film thickness (δ) was reported [8].

This paper continues our work on the impact dynamics of two-component droplet wall-film interactions using hyspin and hexadecane. The focus here is to provide a unified treatment of the crown-type splashing phenomena by analysing the splashing outcome in quantitative terms. A systematic experimental study is therefore carried out to determine characteristic crown parameters, such as crown height and diameter, the maximum number of liquid fingers and the number, size and average velocity distribution of the secondary droplets as function of We_D and δ. These data can then be used to validate numerical simulations, derive input parameters and/or to improve technical applications. Based on the hyspin-hexadecane splashing limit ($We_D^{5/8} Oh_{ave}^{-1/4} = 114 + 163\delta^{5/6}$), published in our previous work [8], we vary the Weber number in the range of $500 < We_D < 1600$ and dimensionless film thickness between $0.05 < \delta < 0.5$. The analysis shows a very consistent behaviour independently of the choice of liquid combinations. Deviations in the crown evolution or in number, velocity and size of secondary droplets are always associated to the changes in the crown dynamics (e.g. rim contraction). The present paper is organized as follows. Section 2 describes the experimental setup and procedure, the image processing and defines the experimental parameter range. Section 3 reports experimental results on the impact morphology (3.1), evolution of crown parameters (3.2) and crown characteristics (3.3), number of secondary droplet (3.5), size of secondary droplets (3.5.3) and velocity of secondary droplets (3.5.4) as function of We_D and δ.

2. Experimental methodology

2.1. Test Rig

[Figure 2 about here.]

The experimental setup has been described in details in earlier publications, e.g. [8], thus only a brief overview will be given. The setup consists of the droplet generation system, the impingement area and the two-perspective imaging system (front and side view). A schematic representation of the test rig is shown in Figure 2. The droplets are generated by a dropper. A small pump of constant volumetric flow rate delivers the liquid to the dropper exit, generating one droplet roughly every 5 s. The cross-sectional area of the dropper exit provides droplets of 2.5 ± 0.1 mm. Adjusting the maximum falling height, the droplet velocity at the point of impact is about 4.5 m/s. A variation of impact velocity is obtained by modifying the distance of the dropper from the impingement area. The impingement area consists of a smooth sapphire glass plate on which a temporary bath is generated by installing thin metallic rings of 0.5 mm or 1.2 mm height. The resulting basin (diameter 60 mm) is then filled with a measured amount of liquid, so that a wall-film of defined thickness is generated. The thickness of the wall-film is determined

with the confocal-chromatic-imaging (CCI) technique using a Micro-Epsilon device (Model: IFC2451 controller and IFS2405-3 sensor). The error in the film height measurement was found to be less than 1 % over the complete range of thicknesses [8]. The two-perspective imaging system allows the observation of drop impact from two different viewing angles (front and side view) to evaluate the symmetry of the impact morphology. The impingement area is thus illuminated from two directions and the respective shadowgraph images are then redirected, so that both images are projected next to each other on the sensor of a Photron Fastcam SA1.1 high speed camera. The drop impacts are recorded for 2 s at 20 kHz with a field of view of 896×320 pixels. The magnification factor M of the two-perspective imaging system is 1:4, which corresponds to an effective optical resolution of 80 $\mu m/pixel$. Thus, very small droplets can be captured and analysed during the post-processing. To trigger the imaging system a laser light barrier was used as shown in Figure 2.

2.2. Image Processing

The properties of the drop prior to impingement, the parameters of the crown and the properties of the secondary droplets are determined from the video sequences using an in-house image processing tool implemented in MATLAB. To confirm the symmetry of the impact, both partial pictures (front and side view) are analysed.

The primary droplet characteristics, e.g. D and U, are calculated from consecutive images of a predefined picture range, in which the droplet is in the area of focus. The procedure is described in detail in our previous work [8]. The uncertainty in D and U was estimated to be less than 2 %.

[Figure 3 about here.]

In a next step the parameters of the crown, such as its height H_{CR}, its diameters at the upper rim D_{CR} and its base D_{LB} and the maximum number of liquids fingers $N_{finger,max}$ are determined (see Figure 3a). The analysis is carried out as follows for each partial picture of the predefined picture range. As a first step the grey-scale images of the video sequence are transformed into binary images, which depict the crown as a filled white structure. Then the crown contour for every line of pixels is determined (see green contour line in Figure 3b) from the binary image. Note that due to the high contrast between crown and background (see Figure 3(a) and (b)) the determination of the crown contour is nearly independent of the threshold settings used for the transformation from grey-scale to binary image. Geppert et al. [8] reported that varying the threshold value results in an error smaller than 1%. At the bottom of the crown contour the endpoints of the crown base are determined (see Figure 3b) and the diameter of the crown base D_{LB} is calculated as the difference in their x-coordinates. The corresponding y-value for the crown base is later on used to determine the crown height. The location of the crown rim is determined by analysing the number of adjacent located

white pixels in each horizontal pixel-line in the image. At the upper crown rim, where the fingers emerge, the line of adjacent white pixels is interrupted. Hence, the last line of continuous white pixels is defined as crown rim (see Figure 3b). Here again the endpoints are determined and the subtraction of their x-values gives the crown rim diameter D_{CR}. The height of the crown H_{CR} is determined by subtracting the y-values of crown rim and crown base.

For the counting of the liquid fingers, a minimum detection height represented by the yellow line in Figure 3b) is defined. Its position results from the actual crown height H_{CR} plus a predefined minimum finger height l_{min}. This minimum finger height ensures a correct counting of the liquid fingers by excluding crown rim disturbances, which do not develop into liquid fingers (a detailed explanation is provided in Section 3.1). To determine the value of l_{min}, the progression of N_{finger} up to $N_{finger,max}$ was evaluated for selected experiments and different l_{min} between $2 < l_{min} < 7$ and compared to the results of a manual count. The best agreement between automated and manual count was achieved for $l_{min} = 5$. Thus, this value was used to obtain the results presented in the following. For all time steps and both partial pictures, all lines of pixels above the detection height are searched for their number of liquid fingers. The largest number of liquid fingers is defined as the maximum number of liquid fingers per partial picture. The total maximum number of liquid fingers $N_{finger,max}$ for each experiment is defined as the maximum of all partial pictures and time steps. The uncertainty of the finger counting algorithm was determined by comparing its results with a manual counting. In total 48 experiments were considered and the uncertainty was found to be ± 3 fingers.

The total number of secondary droplets $N_{drops,max}$ and their size distribution are evaluated employing a counting frame, as shown in Figure 3c. The counting frame is positioned in a way that it encloses all secondary droplets at the beginning of their ejection. Its position is kept constant for the complete analysis of the video sequence. Again both partial pictures are considered. The ejected secondary droplets are counted and their diameter is determined, as soon as they cut across the counting frame. For the last picture of each experiment the droplets remaining inside the counting frame are evaluated, too. The determined values for the number of secondary droplets N_{drops} and their corresponding diameters for each time step and each partial picture are stored in a data array. The total number of secondary droplets $N_{drops,max}$ per experiment is defined as the maximum number counted for each partial image.

The secondary droplet velocity vectors are determined with PTV algorithms [3] also implemented in MATLAB. Particle image velocimetry is a technique that is used to measure the trajectories and velocity magnitudes of moving particles. The secondary droplets generated during the drop impact are treated as the moving particles under consideration. Their trajectory and velocity magnitude are determined from consecutive image pairs of the high speed video. Then, knowing the travel distance and the acquisition rate the instantaneous velocity vector for each secondary droplet (tracked particle) was determined. Note that only droplets with a positive y-velocity component (upward direction) were considered, in order to increase the

accuracy of an average estimated upward velocity. The algorithm makes use of binary intensity matrices in order to determine the centroids of the secondary droplets. The area of interest is selected to be directly at the top of the crown, where the ejection of secondary droplets is initiated, as shown in Figure 3c. The uncertainty in the evaluation of secondary droplet velocity magnitude was estimated to be less than 4 %. This accounts also for droplets which are travelling aligned to the field-of-view and their realistic travelling distance depends on the distance travelled in the direction of field-of-view.

2.3. Test Liquids

[Table 1 about here.]

The present study focuses on the two-component interactions of n-hexadecane $C_{16}H_{32}$ (long-chain alkane) and hyspin AWS 10 (hydraulic oil). The physical properties of these low surface tension liquids are summarised in Table 2. Note that the viscosity of Hyspin is about five times larger than that of hexadecane, while the remaining liquid properties are almost similar. The basic system is a hyspin droplet impacting on a hexadecane wall-film and the reverse system consists of a hexadecane droplet and a hyspin wall-film. For comparison purposes, the corresponding one-component interactions (droplet and wall-film consist of same liquid) are also examined. All employed liquid combinations are listed in Table 3, as well as the corresponding averaged Ohnesorge numbers $Oh_{ave} = (\mu_{ave})/(\sqrt{D\rho_D\sigma_D})$.

[Table 2 about here.]

A number of experiments were carried out over a wide range of impact conditions varied between 0.05 and 0.5 for the normalized film thickness $\delta = h/D$ and, between 500 and 1600 for the drop Weber number $We_D = (\rho U^2 D)/(\sigma)$. The final test matrix consisted of 400 different drop impact experiments. In practice, the wall-film thickness was varied and the droplet diameter kept constant to achieve different values for δ. The Weber number was varied by changing the drop fall height and hence, its final impact velocity.

3. Results and discussion

3.1. Morphology of Crown-Type Splashing

The splashing morphology for the investigated two-component, and the associated one-component interactions, is shown exemplary for $\delta = 0.2$ and $We_D > 1300$ in Figure 4.

[Figure 4 about here.]

The image sequences for all cases show the characteristic crown-type splashing, with the development of liquid fingers along the crown rim and their subsequent break-up into secondary droplets. The first picture of every sequence shows the crown evolution at an early stage after impact ($\tau < 3$). Looking at the

hyspin/hexadecane interaction (1a), disturbances along the crown rim are clearly visible, while for the hexadecane/hyspin interaction (2a) the crown rim is almost undisturbed. This effect is even more pronounced for the one-component interactions. For the low-viscosity liquid hexadecane (3a) the development of fingers has already started, whereas for the high-viscosity liquid hyspin (4a) the crown rim is still undisturbed. Hence, an increase of wall-film viscosity results in a delayed onset of fingering, and therefore, crown-type splashing. Considering the second picture of each sequence, this is further supported by the fact that for hyspin/hexadecane (1b) and the hexadecane one-component interaction (3b) the liquid fingers already break-up into secondary droplets at $\tau \approx 6$, while for hexadecane/hyspin interaction (2b) and the hyspin one-component interaction (4b) this process is just initiated. The first two pictures of the hyspin/hexadecane (1a, 1b) and hexadecane one-component interaction (3a, 3b), also show that not all disturbances visible during the early stage of crown evolution develop further into liquid fingers. Hence, for the correct detection of the number of liquid fingers a minimum finger height l_{min} has to be defined to exclude these disturbances, as already described in Section 2.2. Looking at the remaining three pictures (c-e) of every sequence, the difference in crown shape and evolution, depending on the liquid properties, is clearly visible. The hyspin/hexadecane crown develops a cylindrical shape during the ascending phase (1b). In the receding phase the crown rim starts to contract (1c). As a result, the liquid fingers are melted together (1d) until the crown finally collapses (1e). By contrast, the crown of the hexadecane/hyspin interaction develops a V-shaped (or conical) contour (2b), which is preserved during the receding phase (2c-d). The liquid fingers are elongated during crown receding and persist after the descent of the crown (2e). Taking into account the impact morphologies of the one-component interactions, a similarity between two-component and one-component interactions can be established on the basis of the wall-film characteristics. The hexadecane one-component interaction shows a cylindrical crown shape (3b) and a strengthened crown rim contraction (3d), leading to the formation of a closed bubble (3e). However, the hyspin one-component interaction reveals a V-shaped crown (4b) and also the liquid fingers persist after crown descent (4e). The similarity for Figure 4 row 1 and row 3 or Figure 4 row 2 and row 4 suggests that the crown evolution is mainly dominated by the wall-film liquid. It can be therefore concluded that the properties of the wall-film strongly influence the impact morphology of the two-component interactions, which is in agreement with Banks et al. [2]. Note that, the observed differences in the receding phase of the crown make it necessary to stop the counting of liquid fingers before crown collapse or complete crown rim contraction (prior to pictures 1e-4e in Figure 4). Otherwise the results are not comparable.

3.2. Evolution of characteristic crown parameters

A quantitative evolution of the characteristic crown parameters is presented in this paragraph. The considered crown parameters are the diameter at the upper rim of the crown D_{CR}, the height of the crown H_C and the diameter at the base of the crown D_{LB} (cf. Figure 3a).

[Figure 5 about here.]

In Figure 5 the evolution of the dimensionless crown rim diameter D_{CR}/D (upper graph) and the dimensionless crown height H_C/D (lower graph) are depicted exemplary for the experiments shown in Figure 4. They are plotted against the dimensionless time $\tau = (tU)/D$. In the upper graph of Figure 5 the evaluation range for the analysis of the number of fingers is marked, too.

In general, the evolution of the crown rim diameter D_{CR}/D in time follows a parabolic trend, reaching a maximum value at about $10 < \tau < 15$ for all cases, while the liquid properties, especially the viscosity of the wall-film, influence the height and the width of the parabolas. Considering the two-component interactions, the hexadecane/hyspin interaction (green line) reaches a larger value for $(D_{CR}/D)_{max}$ compared to the hyspin/hexadecane interaction (cyan line). This implies that a decrease in wall-film viscosity results in a decrease in $(D_{CR}/D)_{max}$. Furthermore, this effect is linked to the observed crown shapes (cf. Figure 4). The V-shaped crown of the hexadecane/hyspin interaction promotes the growing of D_{CR}/D, whereas the cylindrical shape and the crown rim contraction observed during hyspin/hexadecane interaction restrict it. This effect is even more pronounced when comparing the hyspin (blue line) and hexadecane (red line) one-component interactions. For the low-viscosity liquid hexadecane, the growth of D_{CR}/D undergoes two different stages. At the beginning ($\tau < 2$) D_{CR}/D grows rapidly and with a comparable rate of growth as in the other cases. But for $\tau > 2$ the growth rate of D_{CR}/D slows down dramatically and nearly stagnates. For the one-component interaction of the high-viscosity liquid hyspin again a parabolic progression is observed and the highest value of $(D_{CR}/D)_{max} \approx 6.4$ is reached. The crown is V-shaped, which promotes the growth of D_{CR}/D. Note that to reach a comparable D_{CR}/D as the hexadecane/hyspin interaction ($We_D = 1420$), the hyspin one-component interaction requires a larger amount of kinetic energy ($We_D = 1578$).

The evolution of the dimensionless crown height H_{CR}/D is shown in the lower graph of Figure 5. Regarding the curve progression, again a parabolic shape is observed. The only exception is the hexadecane one-component interaction (red dashed line), which shows an asymptotic progress. This is strongly linked to the observed impact morphologies. Since for the hexadecane one-component interaction the formation of a closed bubble was observed (cf. Figure 1), the asymptotic value of the crown height is the maximum height of the bubble, which is reached as soon as the crown rim contraction is completed. The parabolic shape of the other curves reproduces the advancing and receding of the crown as it is depicted in Figure 4 for the hexadecane/hyspin, hyspin/hexadecane and hyspin one-component interactions. Looking at the height evolution for two-component cases, we see that the crown rim contraction observed for the hyspin/hexadecane interaction (cyan line) decelerates the receding of the crown, which leads to a wider opening angle of the curve. This effect is more pronounced for the hexadecane one-component interaction, where the strengthened crown rim contraction, hence the formation of a bubble, inhibits the receding of the crown. A comparison of the maximum crown heights $(H_{CR}/D)_{max}$ for the two-component interactions (green and cyan line) shows that with

increasing wall-film viscosity the crown height decreases from $(H_{CR}/D)_{max} = 3$ for the hyspin/hexadecane interaction to $(H_{CR}/D)_{max} = 2.7$ for the hexadecane/hyspin interaction. The same trend is observed for the one-component interactions. Despite the higher Weber number of the hyspin one-component interaction ($We_D = 1578$), its maximum crown height ($(H_{CR}/D)_{max} = 3$) stays below the maximum height achieved at the hexadecane one-component interaction ($We_D = 1313$, $(H_{CR}/D)_{max} = 3.4$). Note that the maxima at $(H_{CR}/D)_{max}$ and $(D_{CR}/D)_{max}$ are reached at approximately the same point in time for all cases.
Finally, the evolution of the diameter at the crown base D_{LB}/D (not depicted here) is considered. A comparison of the curve progressions of all four cases shows that up to $\tau = 2$, they have the same tendency. This means that at this early stage the growing of D_{LB}/D is independent of the liquid properties, namely viscosity. It is only driven by inertia and surface tension force, as already discussed by Yarin and Weiss [33]. Due to the higher viscosity of the wall-film, the rate of growth is slowed down at later times for the cases of hexadecane/hyspin and hyspin one-component interaction. Moreover, the maxima $(D_{LB}/D)_{max}$ for these cases are smaller compared to the hyspin/hexadecane and hexadecane one-component interactions, which have a low-viscosity wall-film. Hence, an increase in wall-film viscosity leads to a decrease in $(D_{LB}/D)_{max}$.

In summary, an increase in wall-film viscosity leads to a decrease in $(D_{LB}/D)_{max}$ and $(H_{CR}/D)_{max}$, but to an increase in $(D_{CR}/D)_{max}$. This is because with increasing wall-film viscosity the angle between crown and wall-film decreases, changing the direction of liquid propagation from vertical to inclined. This causes the differences in crown shape, i.e. cylindrical (cf. Fig. 4, row 1 and 3) or V-shape (cf. Fig. 4, row 2 and 4). This result is confirmed by the theoretical analysis of Josserand and Zaleski [15], who modelled the early stage of drop impact for one-component interactions as a potential flow everywhere except in the small neck region, where viscosity plays a major role. Additionally, they presented numerical simulations showing the decrease of crown angle with increasing viscosity. Hence, for one- and two-component interactions, the remaining energy is either used to increase the crown height (low viscosity) or the crown rim radius (high viscosity). This influences the formation of liquid fingers along the crown rim and explains the time shift for the onset of fingering. It is shown later that the crown morphology also influences the formation and ejection of secondary droplets.

3.3. Crown characteristics as function of We and δ

The effect of non-dimensional film thickness (δ) and Weber number (We_D) on the characteristic crown parameters is demonstrated in the following. In Figure 6 the maximum crown rim diameter $(D_{CR}/D)_{max}$ is plotted against δ for all investigated liquid combinations. Figure 6a) depicts the results for the two-component interactions and the hyspin one-component interaction. The hexadecane one-component interaction is plotted separately in Figure 6b), giving special emphasis to the influence of bubble formation. Hence, the dependence on the liquid properties, represented by the Ohnesorge number calculated with average viscosity ($Oh_{ave} = \mu_{ave}/\sqrt{D\rho_D\sigma_D}$) can be evaluated.

[Figure 6 about here.]

The plots show that $(D_{CR}/D)_{max}$ increases with increasing averaged Ohnesorge number Oh_{ave}. For $\delta = 0.1$ the lowest value of $(D_{CR}/D)_{max} \approx 5.5$ is reached for the hexadecane one-component interaction ($Oh_{ave} = 0.0150$), while the hyspin one-component interaction ($Oh_{ave} = 0.0630$) shows the highest values of $(D_{CR}/D)_{max} \approx 7$. The two-component interactions fit in this trend. For the hyspin-hexadecane interaction, which has the slightly lower $Oh_{ave} = 0.0384$, $(D_{CR}/D)_{max} \approx 6$. For the reverse system (hexadecane-hyspin) with $Oh_{ave} = 0.0417$, $(D_{CR}/D)_{max} \approx 6.5$ was measured. The increase of $(D_{CR}/D)_{max}$ with Oh_{ave} results from the fact that the crown evolves form cylindrical to V-shaped with increasing viscosity, as explained above and by Josserand and Zaleski [15].

Considering the two-component interactions and the hyspin one-component interaction depicted in Figure 6a), it can be seen that $(D_{CR}/D)_{max}$ is independent of We_D, but it decreases with increasing dimensionless wall-film thickness δ. The effect of viscosity on the crown angle is reduced with increasing wall-film thickness δ. This means for thicker wall-films only cylindrical crown shapes are observed. On the contrary, the hexadecane one-component interaction shows a dependence on both We_D and δ. In general, as either parameter increases the value for $(D_{CR}/D)_{max}$ decreases, but Figure 6b) shows two different dependencies related to the observed impact morphology. In the case of simple crown formation (filled symbols in Fig. 6b), which is observed for $We_D < 1000$, the influence of We_D and δ on $(D_{CR}/D)_{max}$ is negligible. This changes for $We_D > 1000$, when suddenly an increase in both parameters, We_D and δ, leads to a decrease in $(D_{CR}/D)_{max}$. This behaviour is linked to the crown rim contraction and thereof resulting formation of a closed bubble, which inhibits the growth of the crown rim. In Figure 6b) the open symbols depict the cases for which bubble formation was observed. Comparing the here presented regime to the critical values for bubble formation of Geppert et al. [8] ($We_D > 1200$ and $\delta > 0.2$), which are presented earlier (see Fig. 1), shows a good agreement.

The influence of We_D and δ on the maximum crown height $(H_{CR}/D)_{max}$ is presented in Figure 7. Again the dependence for the hexadecane one-component interaction is presented separately in Figure 7b), while the dependence for the remaining three combinations is summarized in Figure 7a). In general, for all liquids combinations the crown height $(H_{CR}/D)_{max}$ increases strongly with δ. This can be explained due to the increased mass flux in the crown with increasing film thickness. The dependence upon the Weber number is more complex. For liquid combinations containing at least one high viscous liquid, only a weak dependence on We_D is recognizable, see Figure 7a). This is due to the stronger damping of impact kinetic energy by viscous forces. For low-viscosity liquids like hexadecane (Figure 7b)) it is clear that an increase in Weber number leads a higher crown, due to the associated increase in impact kinetic energy.

[Figure 7 about here.]

These findings are in agreement with Cossali et al. [5] who reported that the maximum crown height depends

only on the drop impact velocity for a similar value of Ohnesorge number $Oh = 0.019$. Instead a completely different behaviour is observed at very high Weber numbers in concomitance with the occurrence of the bubble formation. In this case the incoming mass flux is bundle into increasingly thicker liquid fingers (Fig. 4 3d)).

In Figure 8 the influence of We_D and δ on the maximum crown base diameter $(D_{LB}/D)_{max}$ for all investigated liquid combinations is shown.

[Figure 8 about here.]

For the two-component interactions as well as the hyspin one-component interaction $(D_{LB}/D)_{max}$ is only a function of δ. For all three systems $(D_{LB}/D)_{max}$ has a minimum at $\delta \approx 0.15$. Afterwards an increase in δ results in an increase in $(D_{LB}/D)_{max}$. Furthermore, a decrease in wall-film viscosity leads to a slight increase in $(D_{LB}/D)_{max}$ (compare cyan triangles with blue diamonds and green triangles). This is due to the fact that less energy is required to push away a low viscosity wall-film. For the hexadecane one-component interaction, depicted with red squares in Figure 8, $(D_{LB}/D)_{max}$ is also only a function of δ. But due to its lower viscosity, the strong crown rim contraction and the bubble formation, a higher scatter of the $(D_{LB}/D)_{max}$ values is observed.

In general, for all liquid systems, the maximum crown base diameter $(D_{LB}/D)_{max}$ is larger than 4.5 times the diameter of the impinging droplet D. This needs to be taken into account when setting up experimental or numerical investigations, because it defines the required wall-film width.

3.4. Analysis of the number of liquid fingers

In this paragraph the results of the analysis of the maximum number of liquid fingers $N_{finger,max}$, developed during crown-type splashing of the considered liquid combinations, are presented.

[Figure 9 about here.]

The most pronounced influence on $N_{finger,max}$ was determined for the dimensionless film thickness δ. In Figure 9 the maximum number of fingers $N_{finger,max}$ is plotted against δ, for every investigated one- and two-component interaction. For data reduction, all experiments were grouped according to employed liquid combination and dimensionless film thickness δ. The detected maximum numbers of liquid fingers in each group were then averaged. In this averaging process the potential influence of all other parameters is disregarded, since it has only a minor effects [11]. In Figure 9 each coloured symbol represents one of these averaged values, depending on liquid combination and δ. Note that the sparse data set for the hyspin one-component interaction results from the fact that, the splashing limit for this liquid for $\delta \geq 0.3$ requires

$We_D > 1800$, which exceeds the capability of our experimental test rig.

For all investigated liquid combinations $N_{finger,max}$ decreases with increasing δ. This means a thicker wall-film strongly damps the finger formation. That is explained by the fact that for the displacement of a thicker wall-film, more energy is dissipated, which is no longer available for the finger formation. Krechetnikov and Homsy [16] discussed the instability mechanism leading to crown formation. In this context, they determined the number of fingers along the crown rim for two different types of milk ($0.0015 < Oh < 0.0041$ and $60 < We_D < 1400$) and found that it decreases with increasing wall-film thickness. Their experimental data are depicted with black symbols in Figure 9. Despite the difference in Ohnesorge number, their results for milk are in good agreement with our results for alkanes. To describe the decrease of $N_{finger,max}$ as a function of δ for the here presented results a power law fit was applied, which leads to the following correlation for all combinations:

$$N_{finger,cor} = 8.6\ \delta^{-0.26}. \tag{1}$$

In Figure 9 the solid line represents equation 1. The error bars depict the uncertainty of finger counting of ± 3 fingers with regard to the correlation.

3.5. Analysis of Secondary Droplet Properties

In the following the properties of the secondary droplets ejected during drop impact are analysed in terms of We_D and δ. However, the characteristic numbers that were used to described the phenomenon are defined first in Section 3.5.1

3.5.1. Characterisation of Secondary Droplet Properties

For the evaluation of the effect of secondary droplets on technical applications, the total number of ejected droplets $N_{drops,max}$, their volume and size distribution are essential quantities. Employing the relative volume of ejected secondary droplets V_{rel} with respect to the volume of the impinging droplet, enables to quantify the loss of liquid mass from the wall-film. V_{rel} is calculated from the total volume of secondary droplets $V_{secdrops,tot}$ divided by the volume of the impinging droplet $V_{drop,0}$:

$$V_{rel} = \frac{V_{secdrops,tot}}{V_{drop,0}}. \tag{2}$$

To represent the distribution of drops sizes in sprays, for most engineering applications two parameters are employed. One is a representative diameter and the other a measure of the drop size range [17]. Moreover, relating complete droplet-size distributions (i.e.histograms or mathematical distribution functions) to physical processes or product properties is inconvenient. Hence an appropriate data reduction must be carried out. Using mean droplet diameters satisfies both requirements, because they provide the required

information [1]. The general definition of mean droplet diameters is,

$$\overline{D}_{p,q} = \left[\frac{\sum_i N_i \; D_i^p}{\sum_i N_i \; D_i^q} \right]^{\frac{1}{p-q}} \tag{3}$$

where i denotes the considered size range, N_i is the number of drops in size range i and D_i is the middle diameter of size range i [17, 22]. The parameters p and q have usually integer values, which are chosen with respect to the field of application.

For the data reduction presented here the arithmetic mean diameter $\overline{D}_{1,0}$ is selected.

3.5.2. Number of Secondary Droplets and ejected Volume

[Figure 10 about here.]

In Figure 10 the total number of ejected secondary droplets $N_{drops,max}$ is plotted against the dimensionless film thickness δ. Different Weber number regimes are represented by black lines. For the two-component interactions, depicted in Figure 10a, an increase in dimensionless film thickness up to $\delta = 0.2$ leads to a very pronounced decrease of $N_{drops,max}$. For $\delta > 0.2$ the reduction of $N_{drops,max}$ flattens. Regarding the influence of the Weber number, increasing We_D results in an increase of $N_{drops,max}$, as expected.

For the one-component interactions in general the same trends are observed. Even so the database for hyspin is sparse, a decrease of $N_{drops,max}$ with increasing δ is identifiable. Moreover, compared to the less viscous hexadecane one-component interaction $N_{drops,max}$ is much smaller, which is due to the fact that most of the kinetic energy is dissipated by viscous forces. Consequently, significantly less secondary droplets are formed. In the case of the hexadecane one-component interaction a clear decrease of $N_{drops,max}$ with δ is observed, which is more pronounced for $\delta < 0.2$ and flattens for $\delta > 0.3$. This agrees with the results of Cossali et al. [5] for $\delta \geq 0.29$, showing an increase of $N_{drops,max}$ due to an increase in We_D only. As depicted in Figure 10b, the dependence on We_D for our experiments is inconsistent. An increase in Weber number up to $We_D = 1000$ leads to an increase in $N_{drops,max}$. For $1000 < We_D < 1200$, $N_{drops,max}$ drops off to values in the range of $We_D < 800$. For $We_D > 1200$ again an increase of $N_{drops,max}$ with We_D is observed. This inconsistency is strongly linked tot he observed impact morphology (cf. Fig. 4). For $We_D < 1000$ the ejection of secondary droplets proceeds undisturbed before the onset of crown rim contraction. In the intermediate range of We_D the impact energy is high enough to prolong the impact process, so that crown rim contraction takes place. Due to the contraction the crown rim thickens and the liquid fingers merge, which leads to a reduced number of secondary droplets. If $We_D > 1200$ the higher amount of available kinetic energy delays the crown rim contraction, which allows the formation of more secondary droplets. In Figure 10b) also the experiments for which bubble formation was observed are depicted. They show a large scattering range and no clear trend. This results from the different mechanisms of bubble destruction. For example the bubbles with $N_{drops,max} > 100$ at $0.1 < \delta < 0.2$ are destroyed due to the rip off of the

bubble from the wall-film. Thereby, the liquid in the bubble wall is ejected outwards and disintegrates into secondary droplets. In contrast, the bubbles with $N_{drops,max} < 50$ rupture at the top due to the down flow of the liquid. Hence, the bubble collapses into the wall-film, whereby no droplets are ejected. A third mechanisms of bubble destruction, originates from secondary droplets which fall back down, bursting the bubble. Note that for the hexadecane one-component interaction the highest numbers of secondary droplets are counted.

[Figure 11 about here.]

The normalised cumulative volume V_{rel} is plotted against the dimensionless film thickness δ in Figure 11. Again black lines mark the different Weber number ranges. In general, with increasing Weber number V_{rel} increases, because more energy is available for the generation of secondary droplets. However, for the hexadecane one-component splashing a completely different behaviour is observed due to the rim contraction process, which occurs at $We_D > 900$. In this case (Fig 4, row 3) the crown rim shrinks together and induces a significant reduction in the ejected secondary droplets (i.e. V_{rel}), as shown in Figure 11. This effect is further enhanced by the subsequent bubble formation. The variation of V_{rel} is instead inversely proportional to an increase in film thickness. As shown in Figure 6 and Figure 7, for a given Weber number the surface area of the crown increases with the film thickness. This implies that a larger fraction of the initial kinetic energy has been converted in surface energy and therefore is no longer available for the generation of secondary droplets. Consequently, the cumulative volume decreases with δ. In Figure 11b and c V_{rel} exhibits a different dependence upon δ. To understand this apparent anomaly, one must consider the splashing limit at low film thicknesses. With reference to the splashing correlations provided in the introduction, the critical Weber number for the hexadecane one-component and the hexadecane-hyspin interaction is in the order of 700 and 1000, respectively. For these conditions the total duration of the splashing process is significantly shortened, which implies a strong reduction in the cumulative volume of ejected droplets. Finally, note that only for the hyspin-hexadecane interaction (Fig. 11a)) V_{rel} exceeds 1, which means that more liquid is removed from the system than added by the impinging droplet.

3.5.3. Secondary Droplet Diameters

As a first approach we present the influence of the Weber number We_D and the dimensionless film thickness δ on the arithmetic mean diameter $\overline{D}_{1,0}$, calculated from the secondary droplet size distribution of each experiment. The results for $\overline{D}_{1,0}$ are plotted against δ in Figure 12 for each liquid combination separately.

[Figure 12 about here.]

Generally, for the two-component interactions the arithmetic mean diameter $\overline{D}_{1,0}$ increases with increasing dimensionless film thickness δ and it decreases with increasing Weber number We_D. Although the basic system (Fig. 12a)) shows more scatter, especially for $\delta > 0.15$, compared to the clear trend of the reverse system (Fig. 12b)). The scatter observed for the basic system seems to be caused by a stronger influence of the Weber number on the process. This is linked to the choice of wall-film liquid, because a comparison with the one-component interactions depicted in Figure 12c),d) reveals a similar behaviour. Despite the small dataset the one-component interaction of hyspin shows a well-defined increase of $\overline{D}_{1,0}$ with δ. For the hexadecane one-component interaction in contrast a fare more complex trend is observed, which is a combined function of δ and We_D. For small Weber numbers, $We_D < 900$, an increase in δ results in an increase in $\overline{D}_{1,0}$. But, increasing the Weber number up to $We_D = 1200$ leads to a reversing of the trend until for larger values ($We_D > 1200$) $\overline{D}_{1,0}$ gets constant. Again the crown rim contraction is responsible for this behaviour. As shown in the inserted images in Figure 12c) a large amount of small secondary droplets are ejected before crown rim contraction starts (picture 1), while during rim contraction their number is reduced and simultaneously their size increased (picture 2).

3.5.4. Secondary Droplet Velocities

Figure 13 shows velocity histograms and the corresponding weighted average velocity level, $\overline{u}_{drops}$, of the ejected secondary droplets obtained with particle tracking velocimetry (PTV). The histograms are presented for $\delta = 0.2$, while the $\overline{u}_{drops}$ is plotted as a function of the dimensionless film thickness. Note that for the one-component interaction of hyspin, secondary droplet velocities were not possible to be calculated due to peak locking of the PTV algorithm.

Figure 13(a) and (d) show the $\overline{u}_{drops}$ and the associated histograms for two different Weber numbers of the hexadecane one-component interaction. For a given Weber number, the velocity level remains constant as the film thickness δ increases. This is in agreement with 12(c), which shows that for high Weber numbers there is no influence of the dimensionless film thickness δ on the secondary droplet size. On the other side, for a given δ, $\overline{u}_{drops}$ increases from about 1 m/s to 1.8 m/s, as Weber number is increased from 1050 to 1350, respectively. This is to be expected, because of the associated increase in initial kinetic energy with We_D, as can be clearly observed in the histograms in Figure 13(f). In addition the velocity distribution for $We_D = 1350$ shows two distinct peaks, which correspond to two distinct characteristic droplet sizes before and after rim contraction, as shown in Figure 12c. The effect of rim contraction is also visible in the case of hyspin-hexadecane interaction (see Figure13e). They occur at distinctively lower velocity magnitudes (0.2 m/s and 1.6 m/s) due to the increased dissipation of initial kinetic energy for liquid combinations with a high Ohnesorge number. Similarly to the hexadecane one-component interaction, the average velocity magnitude increases with increasing Weber number. However, this trend becomes less

evident as we approach the splashing limit. If we consider the critical Weber number, it increases from 900 to 1000 as δ varies from 0.1 to 0.2. For $\delta = 0.3$ the critical Weber number is equal to 1100 and therefore only the values for $We_D = 1350$ are plotted.
Regarding the hexadecane-hyspin interaction, the velocity distribution reveals only one peak, because when hyspin is chosen as wall-film, no rim contraction in the crown is observed. In compliance to previous remarks the velocity magnitude increases with the Weber number and decreases with the Ohnesorge number. Concerning Figure 13b, a clear trend in the averaged velocity magnitude can not be identified in the chosen range of We_D and δ. This is due to the fact that all these experiments occur rather close to the splashing limit. For example for $\delta = 0.2$ the critical Weber number is of the order of 1025.

[Figure 13 about here.]

4. Summary

Needs to be adapted! This paper presents the results of our pursued work on the impact dynamics of two-component droplet wall-film interactions. We discuss in detail the influence of the droplet impact velocity U, the wall-film thickness h and the liquid properties on the characteristic crown parameters, the number of liquid fingers and the properties of the secondary droplets. Our focus here is on the crown-type splashing regime and therefore a systematic experimental study, consisting of 400 experiments, was carried out. Thereof, this investigation provides a broad experimental database, which can be used to validate numerical simulations, derive input parameters and improve technical applications.
The main conclusion however is that to understand the impact dynamics and thereof correctly simulate them, the impact morphology itself and its influence on the splashing dynamics need to be analysed carefully. For both one- and two-component interactions and $\delta < 0.6$ the viscosity of the wall-film influences the angle between crown wall and wall-film surface. To be precise, the angle decreases with increasing viscosity. As a result the remaining impact energy is either used to increase the crown height (low viscosity, vertical crown ejection) or the crown rim diameter (high viscosity, inclined crown ejection). The occurrence of specific impact phenomena like the formation of a closed bubble, in addition, strongly influences the crown formation, e.g. limiting the maximum crown height and the ejection of secondary droplets.

Acknowledgements

The authors kindly acknowledge the financial support of the Deutsche Forschungsgemeinschaft (DFG).

Appendix

experimental parameters							max. crown parameters				secondary droplet properties			
drop	**film**	**D [mm]**	**U [m/s]**	**h [mm]**	We_D	δ	D_{CR}/D	H_C/D	D_{LB}/D	N_{finger}	N_{drops}	V_{rel}	$\overline{D}_{1,0}$ **[mm]**	$\overline{u}_{drops}$
hexadecane	hexadecane	2.38	4.44	0.493	1313	0.21	4.13	3.42	5.71	13	122	1.85	0.5	Daten
hexadecane	hyspin	2.42	4.47	0.505	1363	0.21	6.08	2.68	5.49	16	47	1.70	0.77	Daten
hyspin	hexadecane	2.30	4.40	0.454	1363	0.20	5.41	2.98	5.50	13	73	2.71	0.72	Daten
hyspin	hyspin	2.54	4.48	0.580	1563	0.23	6.18	2.93	5.34	26	12	Daten	xxx	xxx
etc														

Table 1: Complete experimental datasets for selected experiments of one- and two-component interactions.

Nomenclature

D	impinging drop diameter	$[m]$
D_{CR}	crown rim diameter	$[m]$
D_{LB}	crown base diameter	$[m]$
$\overline{D}_{p,q}$	general definition of mean droplet diameter	$[m]$
$\overline{D}_{1,0}$	arithmetic mean diameter	$[m]$
H_{CR}	crown height	$[m]$
h	wall-film height	$[m]$
K	impact factor, $We^x\ Oh^y$	[-]
l	characteristic length	$[m]$
l_{min}	minimum finger height	$[pixel]$
N_i	number of drops	[-]
N_{finger}	number of liquid fingers	[-]
$N_{finger,max}$	maximum number of liquid fingers	[-]
N_{drops}	number of secondary droplets	[-]
$N_{drops,max}$	maximum number of secondary droplets	[-]
Oh_l	Ohnesorge number, $\mu/\sqrt{\rho\sigma l}$	[-]
p	parameter of mean diameter calculation	[-]
q	parameter of mean diameter calculation	[-]
t	time	$[s]$
U	terminal velocity of impinging droplet	$[m/s]$
u_{drops}	velocity of secondary droplets	$[m/s]$
V_{rel}	relative volume of ejected secondary droplets, $V_{secdrops,tot}/V_{drop,0}$	[-]
$V_{secdrops,tot}$	volume of ejected secondary droplets	$[m^3]$
$V_{drop,0}$	volume of impinging drop	$[m^3]$
We_l	Weber number, $\rho U^2 l/\sigma$	[-]
We_D	Weber number of impinging drop, $\rho U^2 D/\sigma$	[-]
$\overline{We}$	Weber number with averaged liquid properties, $\overline{\rho} U^2 D/\overline{\sigma}$	[-]

Greek letters

δ	dimensionless film height, h/D	$[-]$
μ	dynamic viscosity	$[Pas]$
ρ	density	$[kg/m^3]$
σ	surface tension	$[Nm^{-1}]$

τ	dimensionless time, tU/D_0	[-]

References

[1] Alderliesten, M. (1990). Mean particle diameters. part i: Evaluation of definition systems. *Part. Part. Syst. Charact.*, 7:233–241.

[2] Banks, D., Ajawara, C., Sanchez, R., Surti, H., and Aguilar, G. (2013). EFFECTS OF DROP AND FILM VISCOSITY ON DROP IMPACTS ONTO THIN FILMS. *ATOMIZATION AND SPRAYS*, 23(6, SI):525–540.

[3] Brevis, W., Nino, Y., and Jirka, G. H. (2011). Integrating Cross-Correlation and Relaxation Algorithms for Particle Tracking Velocimetry. *Experiments in Fluids*, 50(1):135–147.

[4] Cossali, G. E., Coghe, A., and Marengo, M. (1997). The impact of a single drop on a wetted solid surface. *Experiments in Fluids*, 22:463–472.

[5] Cossali, G. E., Marengo, M., Coghe, A., and Zhdanov, S. (2004). The role of time in single drop splash on thin film. *Experiments in Fluids*, 36(6):888–900.

[6] Deegan, R. D., Brunet, P., and Eggers, J. (2008). Complexities of Splashing. *Nonlinearity*, 21:1–12.

[7] Gao, X. and Li, R. (2015). Impact of a single drop on a flowing liquid film. *Physical Review E*, 92(053005).

[8] Geppert, A., Chatzianagnostou, D., Meister, C., Gomaa, H., Lamanna, G., and Weigand, B. (2016a). Classification of impact morphology and splashing/deposition position limit for n-hexadecane. *Atomization Sprays*, 10.1615/AtomizSpr.2015013352(26):983–1007.

[9] Geppert, A., Gomaa, H., Meister, C., Lamanna, G., and Weigand, B. (2014). Droplet wall-film-interaction: Impact morphology and splashing/deposition boundary of hyspin/ n-hexadecane two-component system. *ILASS-Americas, 26th An. Conf. on Liquid Atomization and Spray Systems, Portland, Oregon, USA*.

[10] Geppert, A., Greif, F., Lamanna, G., and Weigand, B. (2013). Phenomenology of two-component droplet-wall film-interaction. *ILASS-Europe, 25th Euro. Conf. on Liquid Atomization and Spray Systems, Chania, Greece*.

[11] Geppert, A., Strcbac, A., Marengo, M., Lamanna, G., and Weigand, B. (2015). Two-Component Droplet Wall-Film Interaction: Crown Morphology as a Function of Liquids Viscosity and Surface Tension. *ICLASS 2015, 13th International Conference on Liquid Atomization and Spray Systems*.

[12] Geppert, A., Terzis, A., Lamanna, G., Marengo, M., and Weigand, B. (2016b). On the formation of secondary droplets from crown bottom breakdown during drop impact on very thin films. *ILASS - Europe, 27th Euro. Conf. on Liquid Atomization and Spray Systems, Brighton, UK*.

[13] Guildenbrecher, D. R., Engvall, L., Gao, J., Grasser, T. W., Reu, P. L., and Chen, J. (2014). Digital in-line holography to quantify secondary droplets from the impact of a single drop on a thin film. *Experiments in Fluids*, 55(1670).

[14] Huang, Q. and Zhang, H. (2008). A study of different fluid droplets impacting on a liquid film. *Petroleum Science*, 5:62–66.

[15] Josserand, C. and Zaleski, S. (2003). Droplet splashing on a thin liquid film. *AIP Physics of Fluids*, 15:1650–1657.

[16] Krechetnikov, R. and Homsy, G. H. (2009). Crown-forming instability phenomena in the drop splash problem. *Journal of Colloid and Interface Science*, 331:555–559.

[17] Lefebvre, A. H. (1989). *Atomization and Sprays*. Hemisphere Publishing Corporation.

[18] Liang, G. and Mudawar, I. (2016). Review of mass and momentum interactions during drop impact on a liquid film. *International Journal of Heat and Mass Transfer*, 101:577–599.

[19] Moreira, A. L. N., Moita, A. S., and Panão, M. R. (2010). Advances and challenges in explaining fuel spray impingement: How much of single droplet impact research is useful? *Progress in Energy and Combustion Science*, 36(5):554–580.

[20] Motzkus, C., Gensdarmes, F., and Géhin, E. (2011). Study of the coalescence/splash threshold of droplet impact on liquid films and its relevance in assessing airborne particle release. *Journal of Colloid and Interface Science*, 362(2):540–552.

[21] Motzkus, C., Ghin, E., and Gensdarmes, F. (2008). Study of airborne particles produced by normal impact of millimetric droplets onto a liquid film. *Experiments in Fluids*, 45:797–812.

[22] Mugele, R. A. and Evans, H. D. (1951). Droplet size distribution in sprays. *Industrial and Engineering Chemistry*, 43(6):1317–1324.

[23] Okawa, T., Shiraishi, T., and Mori, T. (2006). Production of secondary drops during the single water drop impact onto a plane water surface. *Experiments in Fluids*, 41(6):965–974.

[24] Pan, K.-L. and Hung, C.-Y. (2010). Droplet impact upon a wet surface with varied fluid and surface properties. *Journal of Colloid and Interface Science*, 352(1):186–193.

[25] Rein, M. (1993). Phenomena of liquid drop impact on solid and liquid surfaces. *Fluid Dynamics Research*, 12:61–93.

[26] Roisman, I. V., Horvat, K., and Tropea, C. (2006). Spray impact: Rim transverse instability initiating fingering and splash, and description of a second spray. *Physics of Fluids*, pages 1–20.

[27] Thoroddsen, S. T., Etoh, T. G., and Takehara, K. (2006). Crown Breakup by Marangoni Instability. *Journal of Fluid Mechanics*, 557:63.

[28] Tropea, C. and Marengo, M. (1999). The impact of drops on walls and films. *Multiphase Science and Technology*, 11:19–36.

[29] Vander Wal, R. L., Berger, G. M., and Mozes, S. D. (2006a). Droplets splashing upon films of the same fluid of various depths. *Experiments in Fluids*, 40(1):33–52.

[30] Vander Wal, R. L., Berger, G. M., and Mozes, S. D. (2006b). The combined influence of a rough surface and thin fluid film upon the splashing threshold and splash dynamics of a droplet impacting onto them. *Experiments in Fluids*, 40(1):23–32.

[31] Walzel, P. (1980). Zerteilgrenze beim Tropfenprall. *Chemie Ingenieur Technik*, 52:1–2.

[32] Yarin, A. L. (2006). Drop Impact Dynamics: Splashing, Spreading, Receding, Bouncing.... *Annual Review of Fluid Mechanics*, pages 1–36.

[33] Yarin, A. L. and Weiss, D. A. (1995). Impact of drops on solid surfaces: self-similar capillary waves, and splashing as a new type of kinematic discontinuity. *Journal of Fluid Mechanics*, 283:1–33.

List of Figures

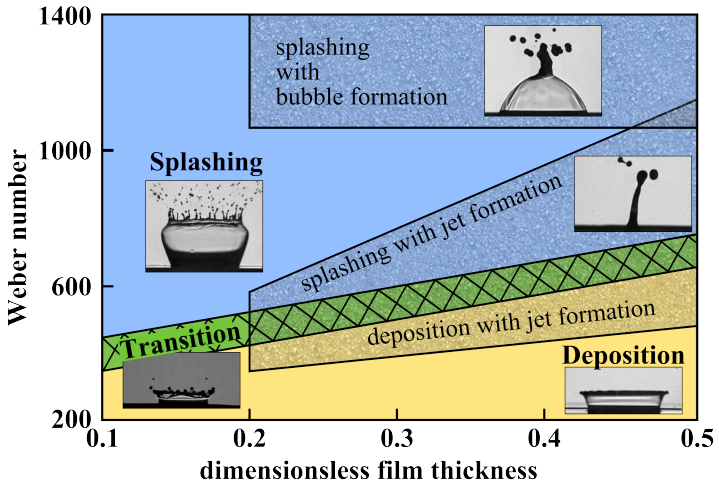

Figure 1: Characteristic map of impact regimes [8]. The yellow area denotes deposition regime, the blue area denotes splashing regime, and the green area denotes transition regime. Additionally, the textured area denote the occurrence of the bubble and jet formation process. Reprinted from Geppert et al. [8] with permission from Begell House, Copyright(2016).

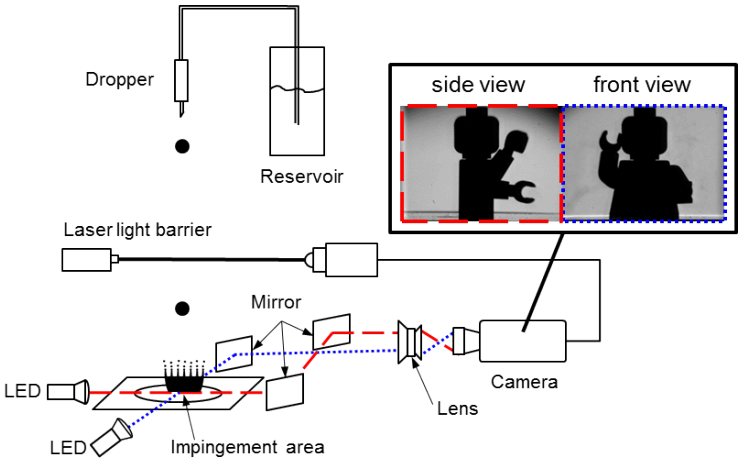

Figure 2: Schematic representation of the experimental setup including exemplary picture of two-perspective image.

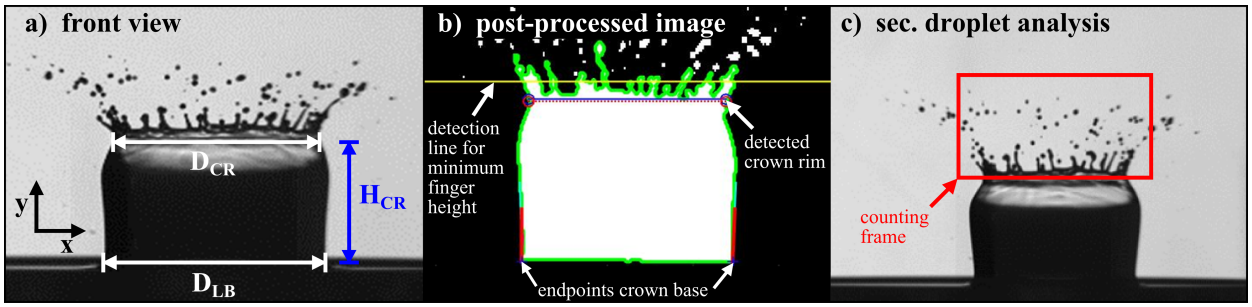

Figure 3: **a)**: Partial picture of a crown developed at hexadecane one-component interaction ($We_D = 1320$,$\delta = 0.2$), including definitions for the crown parameters H_{CR}, D_{CR} and D_{LB}. **b)**: Partial picture after post-processing, including explanations for different detection points. **c)**: Position of counting frame during secondary droplet analysis.

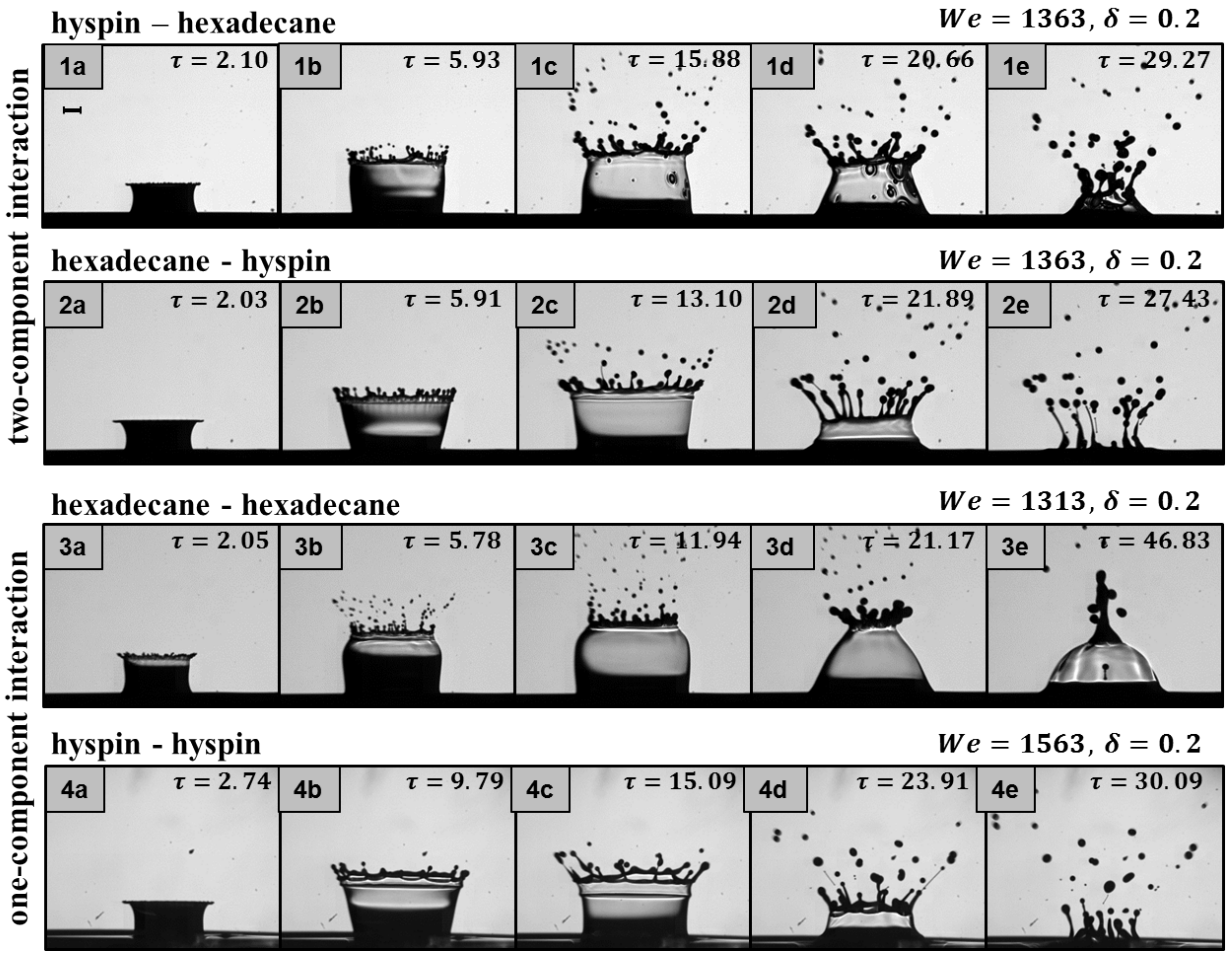

Figure 4: Exemplary image sequences for the morphologies of crown-type splashing observed for the investigated two-component (row 1 and 2) and one-component (row 3 and 4) interactions for $\delta = 0.2$ and $We > 1300$. The values in the upper right corners give the non-dimensional time after impact.

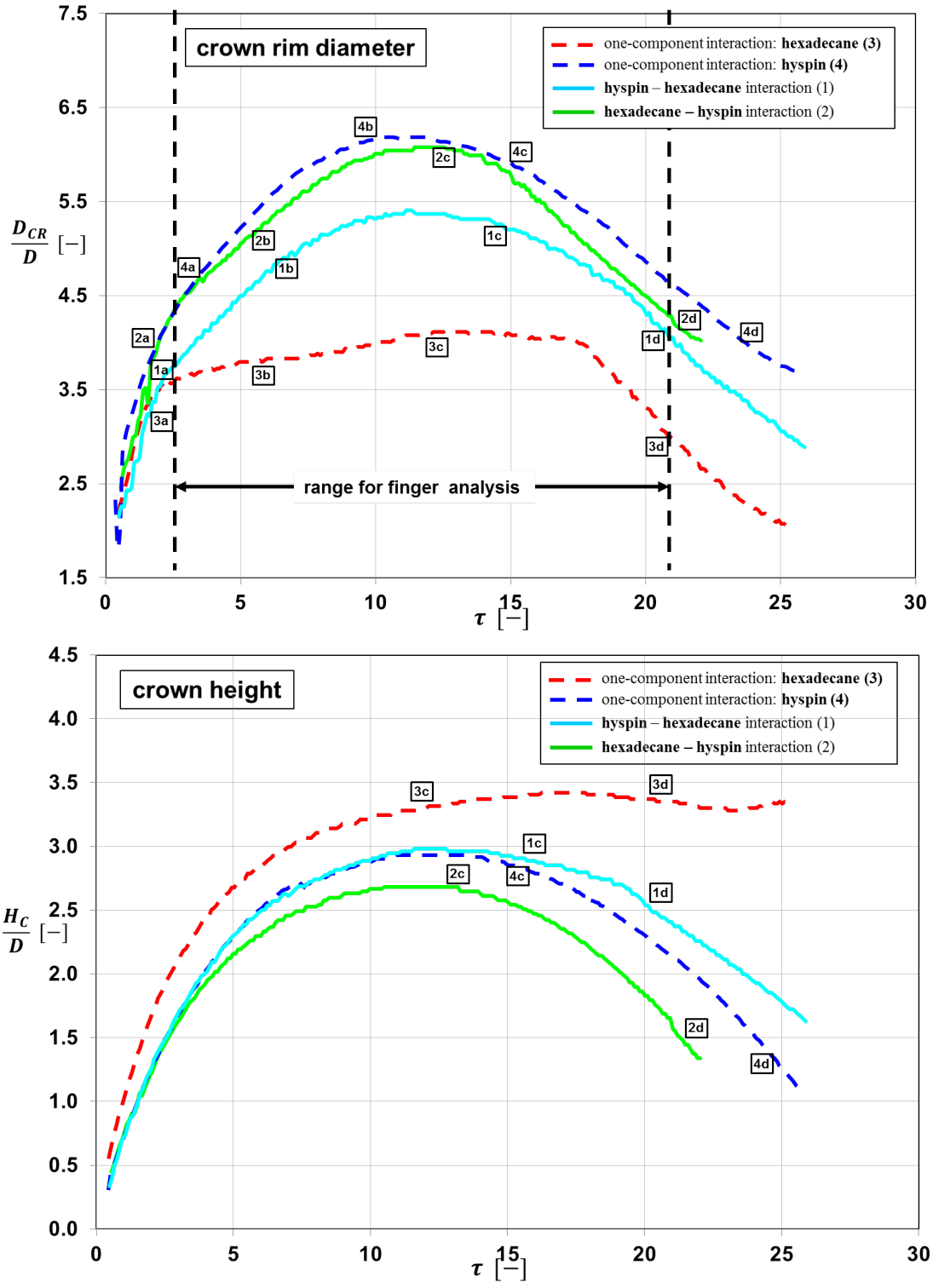

Figure 5: Exemplary plots of the characteristic crown parameters D_{CR}/D (upper graph) and H_{CR}/D (lower graph) as a function of dimensionless time $\tau = (tU)/D$ for the experimental cases discussed in the previous paragraph. The encapsulated numbers refer to the corresponding images in Figure 4.

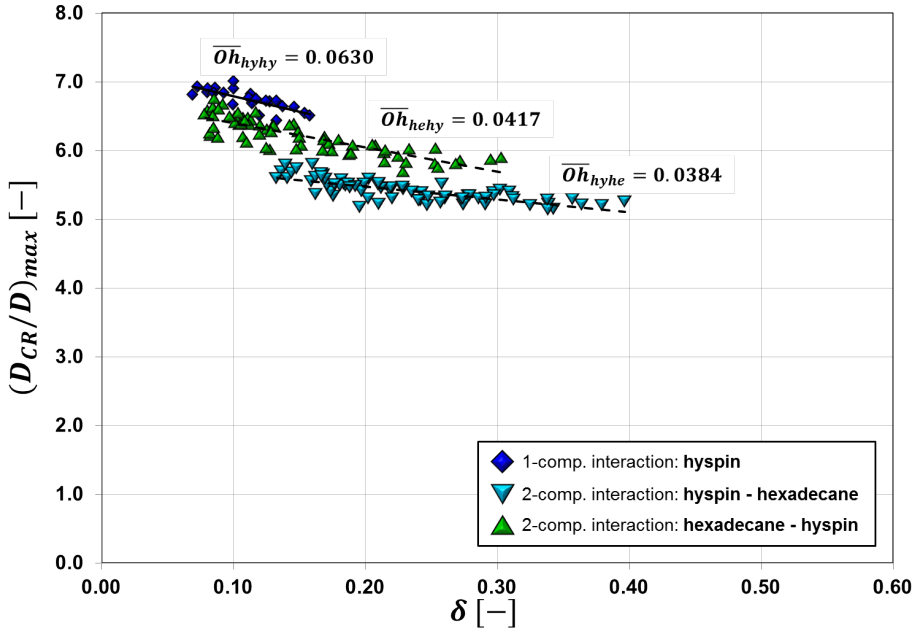

(a) $(D_{CR}/D)_{max}$ as function of δ for two-component interactions and hyspin one-component interaction.

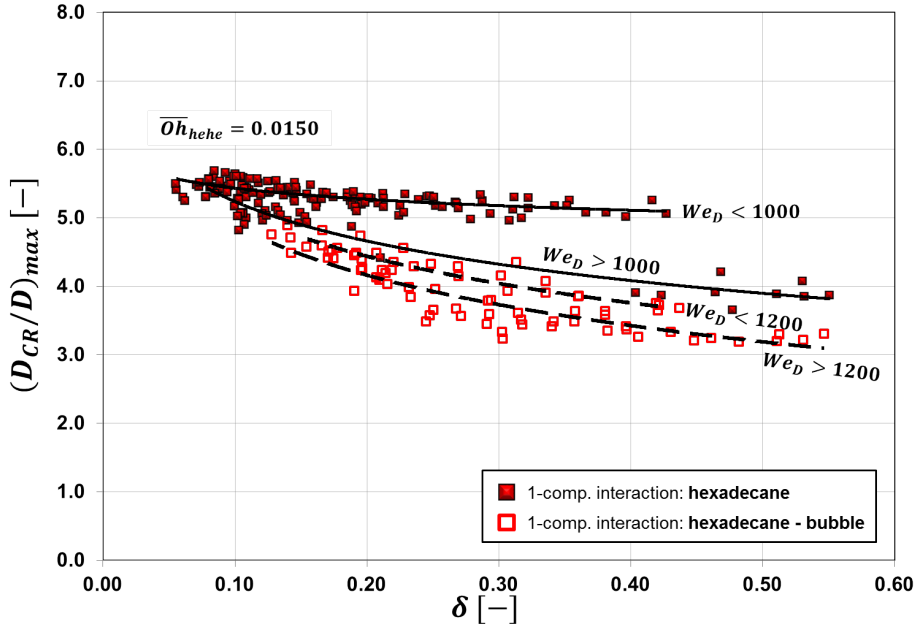

(b) $(D_{CR}/D)_{max}$ as function of δ for hexadecane one-component interaction, showing also the influence of bubble formation.

Figure 6: Maximum crown rim diameter $(D_{CR}/D)_{max}$ as function of experimental parameters Weber number We_D and dimensionless film thickness δ.

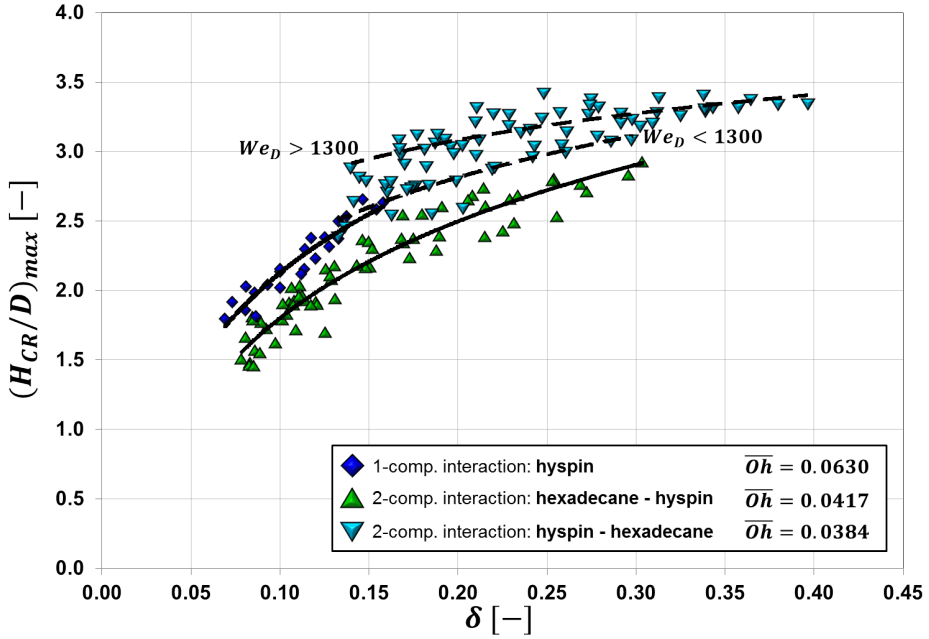

(a) $(H_{CR}/D)_{max}$ as function of δ for two-component interactions and hyspin one-component interaction.

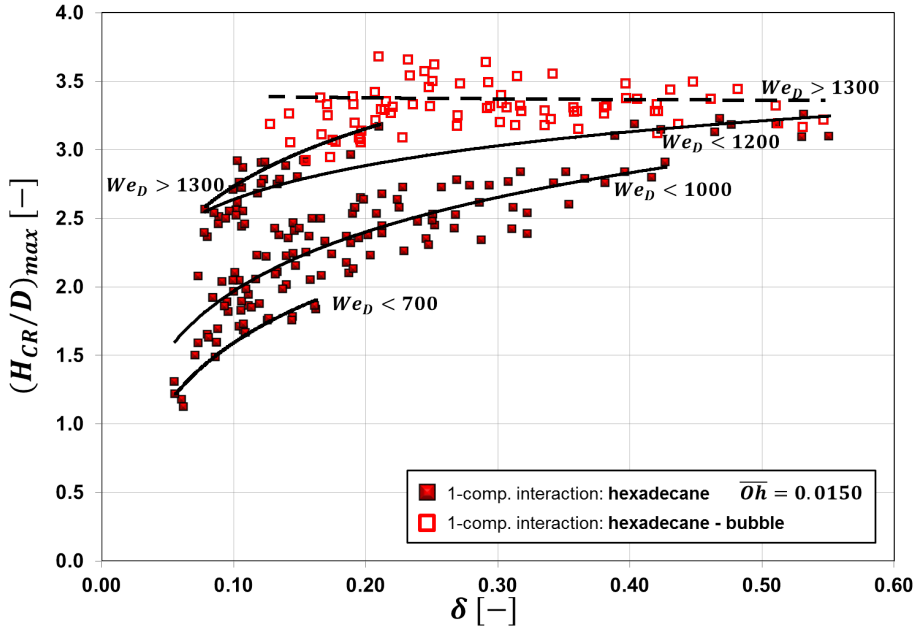

(b) $(H_{CR}/D)_{max}$ as function of δ for hexadecane one-component interaction, also distinguishing between crown formation only and bubble formation.

Figure 7: Maximum crown height $(H_{CR}/D)_{max}$ as function of experimental parameters Weber number We and dimensionless film thickness δ.

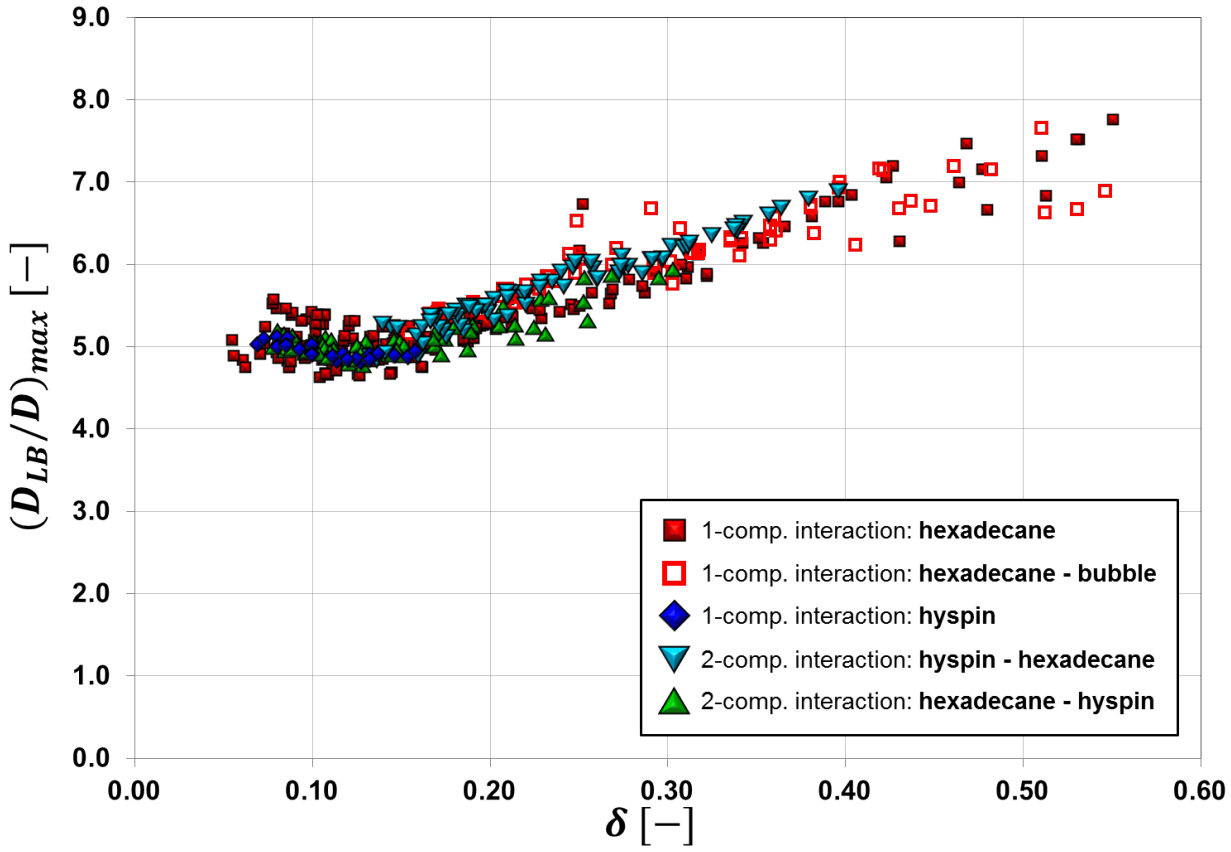

Figure 8: Crown base diameter D_{LB}/D as function of experimental parameters Weber number We_D and dimensionless film thickness δ.

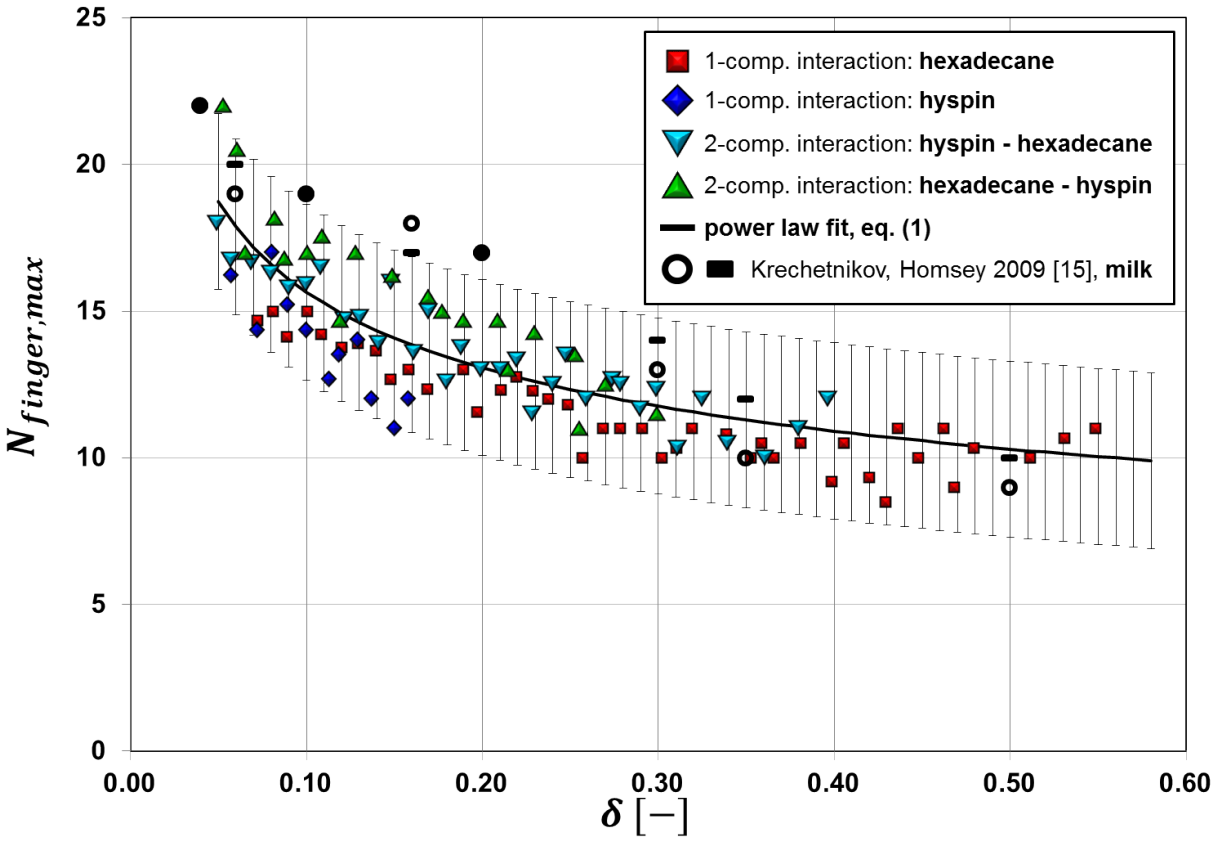

Figure 9: Maximum number of liquid fingers $N_{finger,max}$ as a function of dimensionless film thickness δ. Including power law fit according to equation 1 and uncertainty of finger counting of ± 3 fingers. Black symbols represent experimental data from Figure 2 of Krechetnikov and Homsy [16].

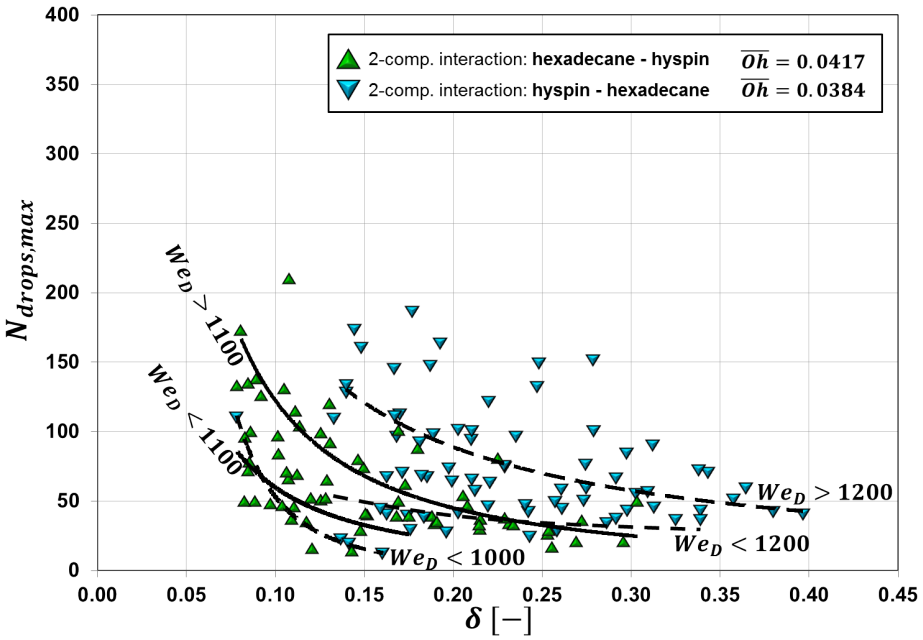

(a) $N_{drops,max}$ for two-comp. interactions

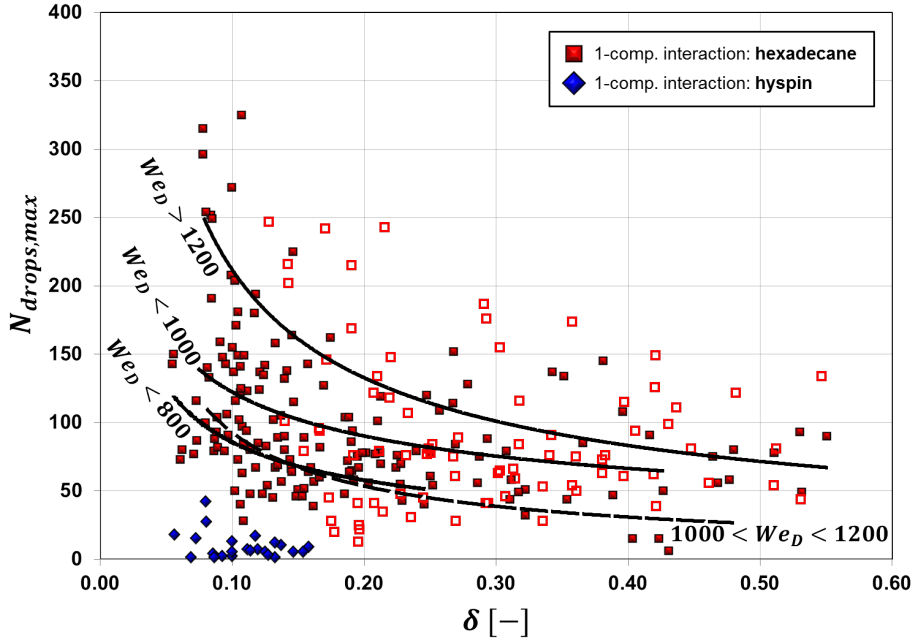

(b) $N_{drops,max}$ for one-comp. interactions

Figure 10: Maximum number of secondary droplets counted as a function of dimensionless film thickness δ. The trend lines show the influence of the Weber number We_D.

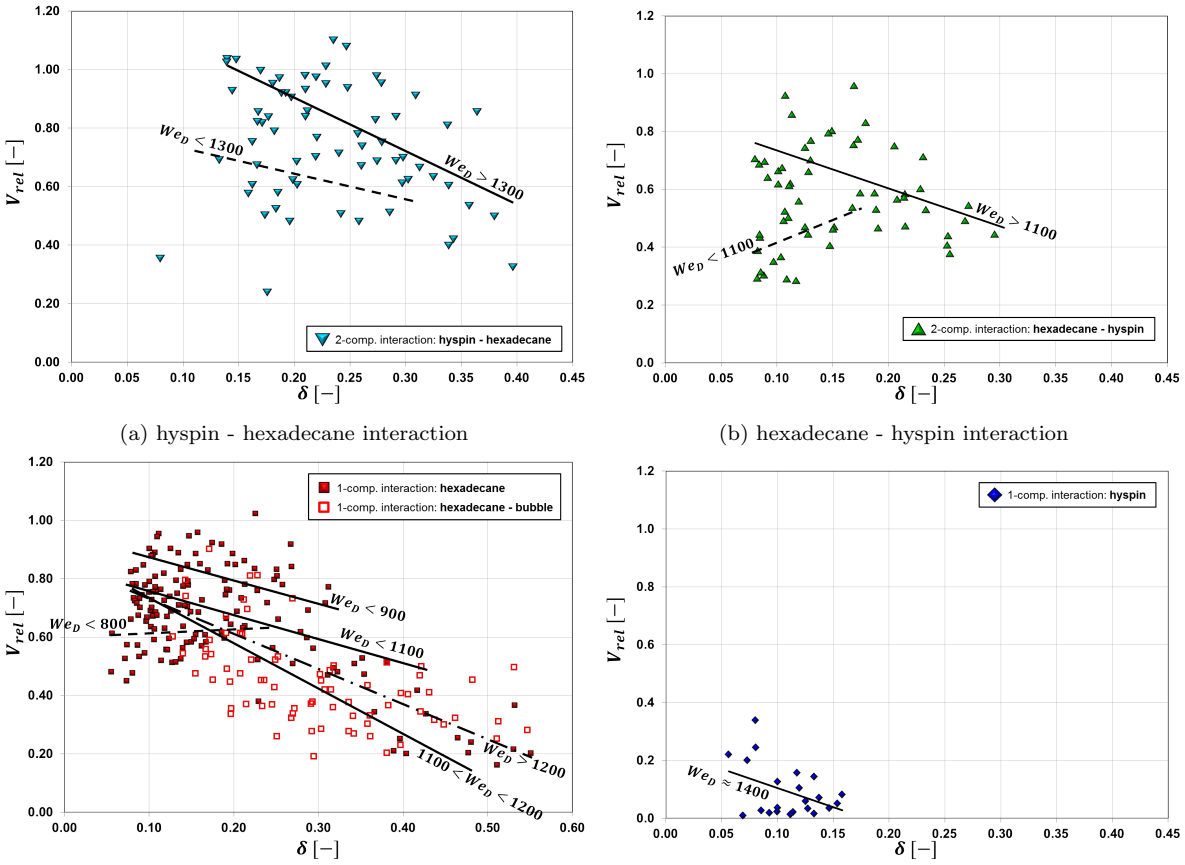

(a) hyspin - hexadecane interaction

(b) hexadecane - hyspin interaction

(c) hexadecane one-comp. interaction

(d) hyspin one-comp. interaction

Figure 11: Ejected volume $V_{rel} = V_{drops,tot}/V_{drop,0}$ normalised by volume of impinging droplet, derived from the droplet size distributions of each experiment.

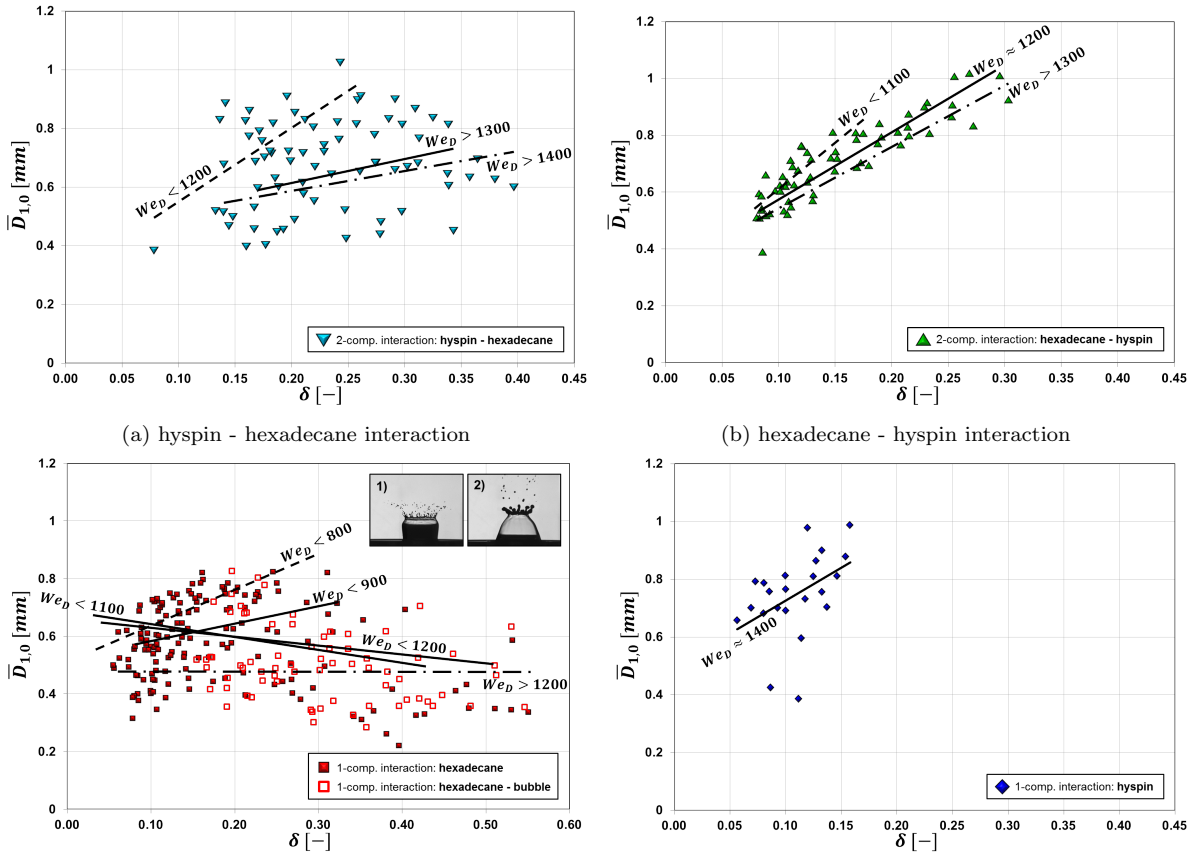

(a) hyspin - hexadecane interaction

(b) hexadecane - hyspin interaction

(c) hexadecane one-comp. interaction

(d) hyspin one-comp. interaction

Figure 12: Arithmetic mean diameter $\overline{D}_{1,0}$ calculated from the droplet size distributions of each experiment.

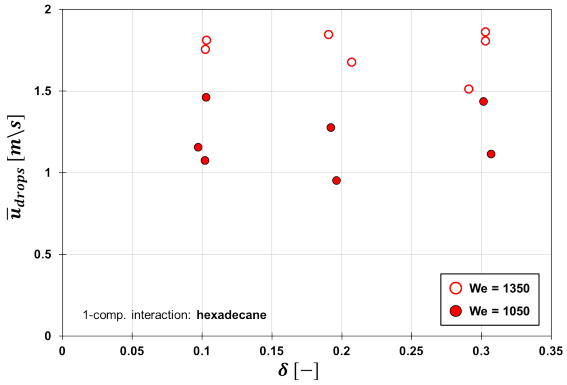

(a) $\overline{u}_{drops}$ for Hexadecane-Hexadecane interaction

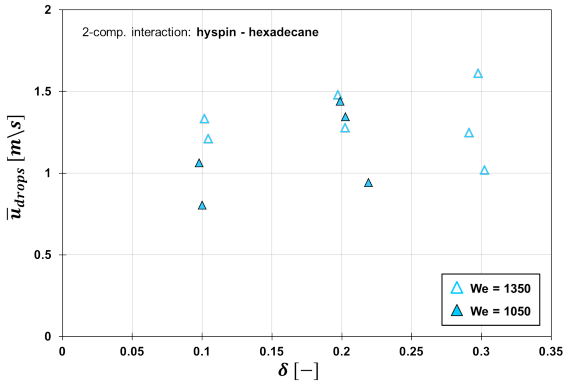

(b) $\overline{u}_{drops}$ for Hyspin-Hexadecane interaction

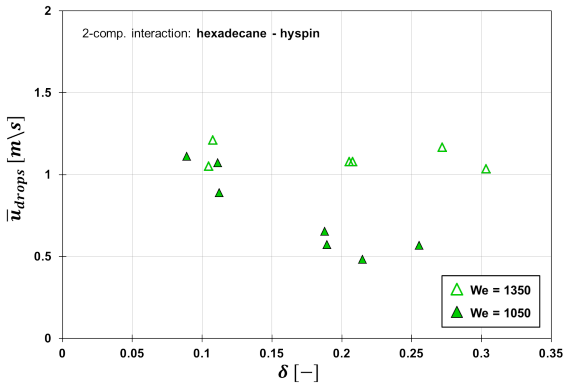

(c) $\overline{u}_{drops}$ for Hexadecane-Hyspin interaction

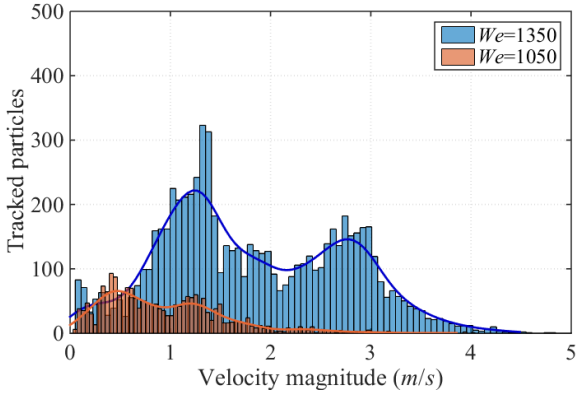

(d) Hexadecane-Hexadecane velocity histogram for δ=0.2

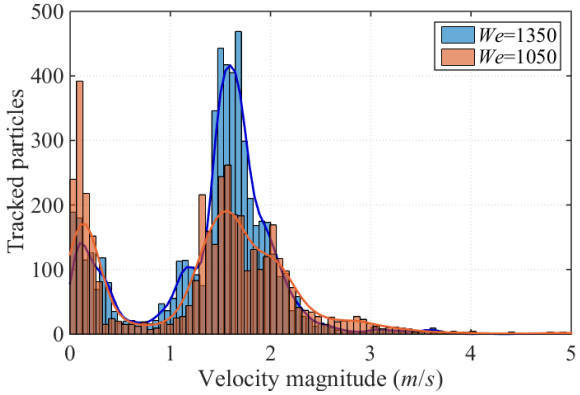

(e) Hyspin-Hexadecane velocity histogram for δ=0.2

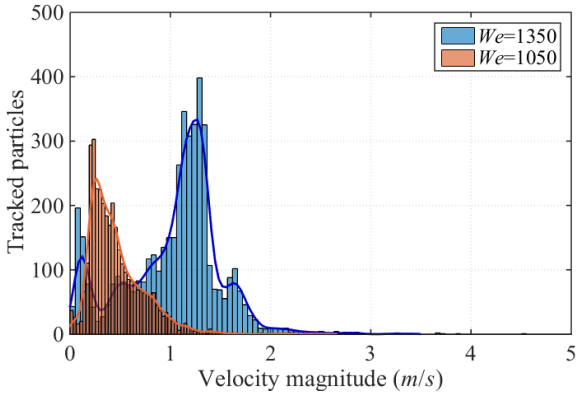

(f) Hexadecane-Hyspin velocity histogram for δ=0.2

Figure 13: Experiment-averaged secondary droplet velocity levels $\overline{u}_{drops}$ and corresponding velocity histograms for selected cases. Top row: $\overline{Oh} = 0.0150$, middel row $\overline{Oh} = 0.0384$ and bottom row $\overline{Oh} = 0.0417$.

List of Tables

Table 2: Physical properties of the test liquids at ambient condition (20°C, 1 bar).

	dyn. viscosity μ $[Pa\,s]$	surface tension σ $[mN/m]$	density ρ $[kg/m^3]$
Castrol Hyspin AWS 10	0.01580	28.65	878
n-Hexadecane $C_{16}H_{32}$	0.00330	27.60	773

Table 3: Investigated liquid combinations and their properties

liquid combination	droplet liquid	wall-film liquid	Oh or Oh_{ave}
hexadecane-hyspin	hexadecane	hyspin	0.0417
hyspin-hexadecane	hyspin	hexadecane	0.0384
1-comp. hexadecane	hexadecane	hexadecane	0.0150
1-comp. hyspin	hyspin	hyspin	0.0630